

Strong Down-Valley Low-Level Jets over the Atacama Desert: Observational Characterization

RICARDO C. MUÑOZ AND MARK J. FALVEY

Department of Geophysics, University of Chile, Santiago, Chile

MARCELO ARAYA

Centro Nacional del Medio Ambiente, Santiago, Chile

MARTIN JACQUES-COPER

Oeschger Centre for Climate Change Research, and Institute of Geography, University of Bern, Bern, Switzerland

(Manuscript received 9 February 2013, in final form 25 July 2013)

ABSTRACT

The near-surface wind and temperature regime at three points in the Atacama Desert of northern Chile is described using two years of multilevel measurements from 80-m towers located in an altitude range between 2100 and 2700 m MSL. The data reveal the frequent development of strong nocturnal drainage flows at all sites. Down-valley, nose-shaped wind speed profiles are observed, with maximum values occurring at heights between 20 and 60 m AGL. The flow intensity shows considerable interdaily variability and a seasonal modulation of maximum speeds, which in the cold season can attain hourly average values of more than 20 m s^{-1} . Turbulent mixing appears to be important over the full tower layer, affecting the curvature of the nighttime temperature profile and possibly explaining the observed increase of surface temperatures in the down-valley direction. Nocturnal valley winds and temperatures are weakly controlled by upper-air conditions observed at the nearest aerological station. Estimates of terms in the momentum budget for the development and quasi-stationary phases of the down-valley flows suggest that the pressure gradient force due to the near-surface cooling along the sloping valley axes plays an important role in these drainage flows. A scale for the jet nose height of equilibrium turbulent down-slope jets is proposed that is based on surface friction velocity and surface inversion intensity. At one of the sites, this scale explains about 70% of the case-to-case observed variance of jet nose heights. Further modeling and observations are needed, however, to define better the dynamics, extent, and turbulence structure of this flow system, which has significant wind-energy, climatic, and environmental implications.

1. Introduction

The Atacama Desert in northern Chile is renowned for its hyperaridity, caused by geographic and climatic factors (Garreaud and Aceituno 2007; Garreaud et al. 2010; Garreaud 2010). To its east, the Andes Cordillera rises to altitudes that exceed 6000 m, precluding moisture transport from the Amazon River basin. To its west, the subtropical southeastern Pacific Ocean (SEP) anticyclone and the cold coastal waters of the Chile–Peru

Current provide for a very stable large-scale environment. The climate of the Atacama Desert is thus characterized by low synoptic variability, very infrequent precipitation, extremely clear skies (except near the coast where stratocumulus are common), intense solar radiation, large diurnal thermal amplitudes, strongly sloping topography, and a very arid surface with little vegetation and negligible moisture availability. In terms of surface winds, these characteristics constitute almost ideal conditions for the observation of terrain-induced thermal circulations. The existence in the Atacama Desert region of near-surface winds driven by the thermal contrasts of the cold ocean, the desert, and the Andes has been described by Schmidt (1999) and documented through short-term field campaigns by Ruttlant and

Corresponding author address: Ricardo C. Muñoz, Dept. of Geophysics, University of Chile, Av. Blanco Encalada 2002, Santiago, Chile.
E-mail: rmunoz@dgf.uchile.cl

Ulriksen (1979) and Ruttlant et al. (2003). These winds have been hypothesized to affect the lower-tropospheric stability and regional hyperaridity (Ruttlant et al. 2003) and the transport of continental aerosols (natural and anthropogenic) toward the SEP stratocumulus layer over the ocean to the west (Chand et al. 2010). Comprehensive and extended datasets describing surface winds in the Atacama Desert have only recently become available, however. Over the last few years, Chilean energy authorities have conducted a series of projects aimed at evaluating the wind-energy potential of the northern part of the country. As part of these efforts, three 80-m meteorological towers with multilevel wind and temperature measurements were installed in the Atacama Desert between 22° and 23°S. The main purpose of this paper is to document the strong nocturnal down-valley flows that were unveiled by these observations. In particular, our objectives are 1) to describe the mean characteristics and variability of the down-valley flow, with special emphasis on the local covariability of wind and temperature profiles at each site, and 2) to provide an observational evaluation of the regional and local controls that affect these flows. The wind-energy implications of these measurements, as well as their numerical modeling and predictability assessment, are being addressed in parallel studies and will be reported elsewhere.

The variability of near-surface winds is affected by factors that span a large range of scales. At the synoptic scale, pressure gradients provide for the day-to-day variability of surface winds, while local obstacles and surface properties determine their finer-grade structure. Between these two scales, regional topography can be a powerful forcing of surface winds, playing a prominent role in shaping their diurnal cycles in connection with mesoscale pressure gradients ensuing from the daytime/nighttime heating/cooling of complex terrain. Whiteman (2000) reviews the basic forms in which this thermal forcing manifests, distinguishing among slope winds, along-valley winds, cross-valley winds, and mountain–plain winds, depending on the temperature contrasts driving the pressure gradients (along a slope, within a valley or between a valley and a plain, across the valley sides, or between a mountain and a plain, for each of the aforementioned cases, respectively). Here we describe the slope-wind and along-valley wind mechanisms, which appear to be most relevant to the flows presented in this work.

Nocturnal slope winds (also referred to as katabatic winds) are driven by an along-the-slope pressure gradient that arises as the air close to an inclined surface cools relative to the air above. Their study has a long history, with various authors considering different additional terms

in the momentum budget to compensate the buoyant downward acceleration. A comprehensive dynamical analysis of this mechanism has been given by Mahrt (1982). In typical conditions, katabatic winds are generally weak and shallow and are considered to be relevant to explaining nocturnal flow down the slope of valley sides. Strong and extensive katabatic flows, however, have been reported over Antarctica (Parish 1982; Parish and Bromwich 1987), where the long polar night, the cold ice-covered surface, and the topography combine to produce regions over which “extraordinary” katabatic winds develop (Bromwich 1989; Wendler et al. 1997). They are characterized by near-surface average speeds between 10 and 30 m s⁻¹ and very high directional persistence. Nocturnal down-slope and down-valley katabatic flows have also been studied in the Rocky Mountains in western North America (e.g., Savage et al. 2008; Whiteman and Zhong 2008). Maximum wind speeds in these cases are generally less than 10 m s⁻¹, with drainage layers that can reach up to ~250 m AGL.

The nocturnal down-valley wind mechanism, on the other hand, does not require an inclined bottom surface at all, as illustrated by the horizontal valley floors used in idealized modeling studies of these flows (e.g., Schmidli et al. 2011). The along-valley pressure gradient driving the surface winds in this case is caused by the relative cooling of the valley’s atmosphere as compared with a nearby plain (Whiteman 1990, 2000). Crucial in this mechanism is the geometric shape of the valley in the cross-valley and along-valley directions, as well as the surface energy budget and radiative effects. Besides their thermal forcing, valley winds can also be affected by large-scale winds and pressure gradients. Whiteman and Doran (1993) categorize these influences in terms of the relationship between the directions of the valley winds and the upper-air (geostrophic) winds, defining the mechanisms of downward momentum transport (with valley winds following closely the upper-air wind direction), forced channeling (with valley winds aligned to the valley axis in the direction of the upper-air wind), and pressure-driven channeling (with valley winds aligned to the valley axis in the direction of the upper-air pressure gradient, perpendicular to the upper-air geostrophic wind).

Although the mechanisms described above appear to be well defined and distinct, real cases in complex terrain will generally be affected by a combination of them. In our case, for example, although the three sites studied are located along valley axes, we cannot discard a priori effects of mountain–plain winds associated with the large Andes Cordillera massif existing to the east or slope-wind effects that are due to the inclination of the valley floors. Therefore, following Whiteman (1990), perhaps a proper

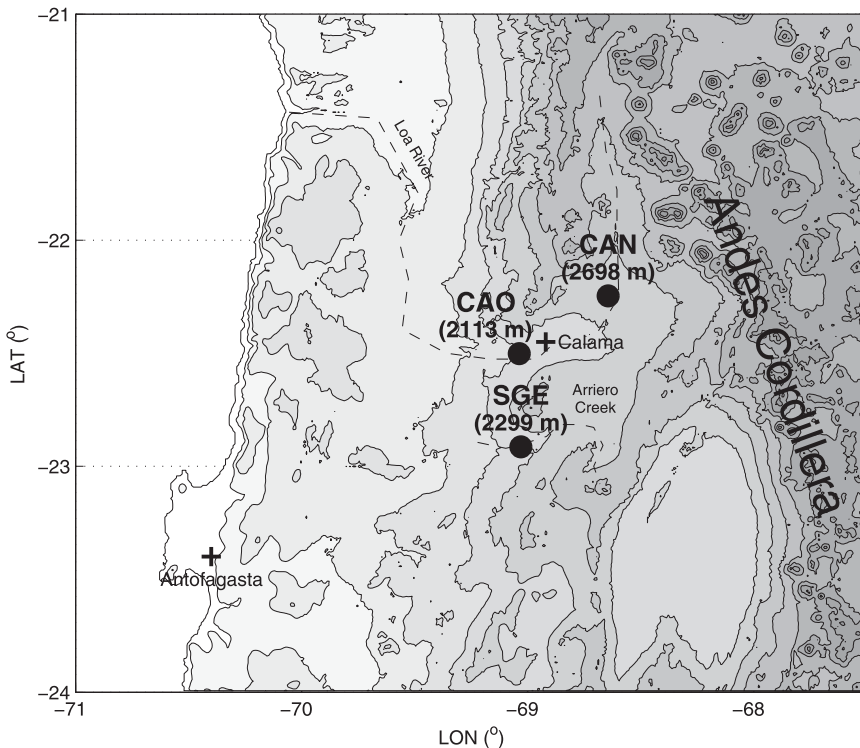


FIG. 1. Topography of the study region and locations of 80-m towers (altitudes of the stations are shown in parentheses). Terrain heights are contoured from 0 to 6000 m MSL every 500 m. Plus signs indicate the radiosonde station (Antofagasta) and the city of Calama. Dashed lines mark the Loa River and Arriero Creek.

name for the nocturnal flows documented here would be the mixed term of drainage winds. We will use the term down-valley winds, however, considering that this is their most persistent direction, and will leave the issue of the dynamical forcing to a discussion in the final part of this paper and to subsequent modeling work.

2. Site and data

a. Regional topography

Figure 1 shows the topography of the study region and the locations of the three 80-m towers analyzed here. All are located along the central axes of wide, gently sloping valleys. Tower SGE is located along Arriero Creek, an east–west-oriented dry streambed close to the town of Sierra Gorda, Chile. Towers CAN and CAO are located along the Loa River valley, up-valley and down-valley of Calama City (~140 000 inhabitants), respectively. At the CAO site the valley is also east–west, whereas at CAN the valley is oriented north–south. Figure 2 shows a closer look at the terrain surrounding the towers, including along- and cross-valley topographical profiles. The average slopes along the valley axes are relatively

steep, with values ranging between 1.3% and 1.7%, and the cross sections show some differences among the three sites. CAN, for example, is located where the Loa River valley widens significantly as compared with the up- and down-valley topography, resulting in a local cross-valley transect with an ~30-km flat floor. In contrast, transects at CAO and SGE show a well-defined U shape, deeper and wider at CAO as compared with SGE. These variations in relief may explain some of the differences that the down-valley winds exhibit at each site, as shown in section 3.

b. Available data

The three towers were installed in February of 2011. Figure 3 provides an overview of hourly wind speeds at 40 m available at the time of this writing. Because the planned measuring period of the towers was limited to 2 yr and our focus of analysis will be the cold season between May and October, the datasets can be considered to be complete for our purposes. Figure 3 shows several gaps in data availability at CAN and CAO. Those in 2011 were mostly due to signal interference of the remote data transmission, which was corrected in August of 2011, whereas the lost month of June in 2012

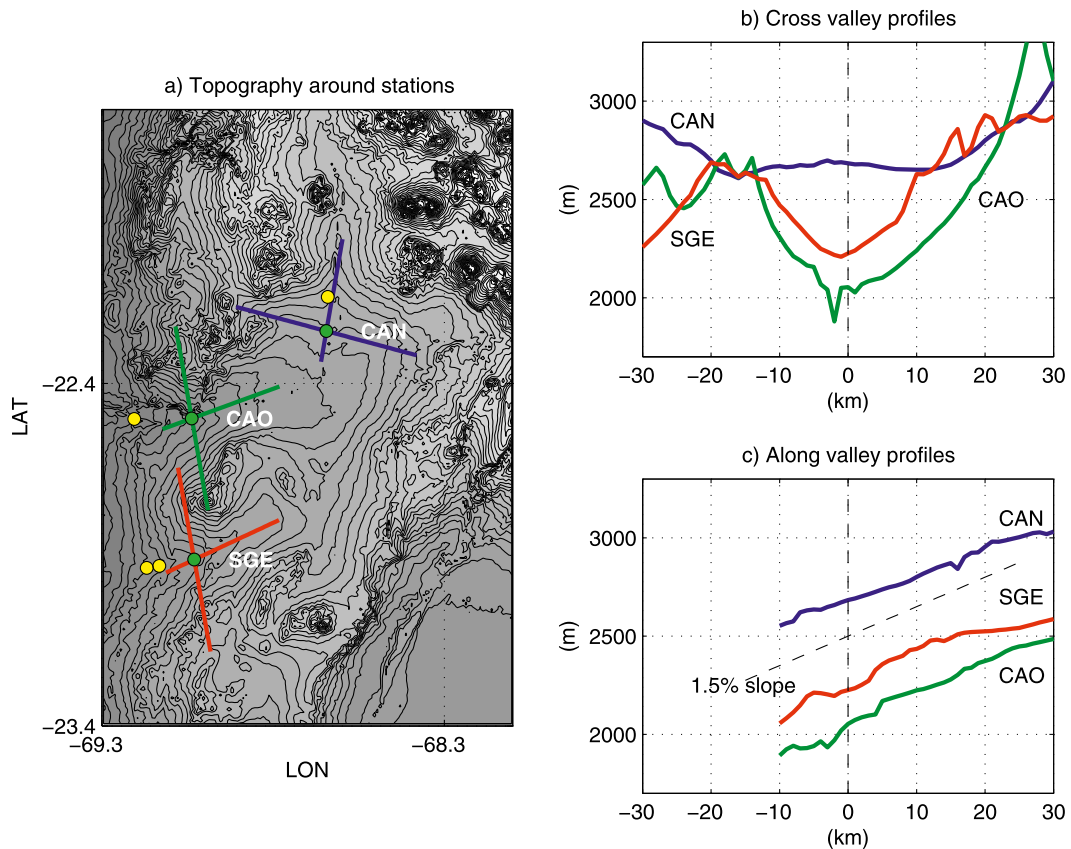


FIG. 2. (a) Topography around the 80-m towers. Lines indicate the locations of the sections that are shown in (b) and (c). Contours are drawn every 100 m. Yellow circles indicate the locations of the 20-m meteorological masts that are referred to later in Fig. 11. (b) Cross-valley topographic profiles around each station. The zero on the abscissa marks the position of the tower. (c) As in (b), but for along-valley topographic profiles. In (a)–(c), stations CAN, CAO, and SGE are denoted by the colors blue, green, and red, respectively.

at CAO was due to vandalism. For the months from May to October, data availability at CAN, CAO, and SGE amounts to 86%, 81%, and 99%, respectively, providing a fair to good representation of winter–spring conditions for 2011–12, which presented weak–moderate La Niña conditions, as indicated by the multivariate ENSO index of Wolter and Timlin (2011).

The main measurements in the towers are wind speed at five levels, wind direction at three levels, and air temperature at three levels (heights and sensors are provided in Table 1). Each of the sensors used included individual calibration certificates against reference standards, making their observations directly comparable among them. Ancillary meteorological data include near-surface relative humidity, atmospheric pressure, and solar radiation; all data are available as 10-min averages computed from 1-Hz samples. As a means of relating the tower measurements to upper-air conditions, we use 1200 UTC (0800 LT) vertical profiles of wind and temperature measured at the operational radiosonde station

of Antofagasta, Chile, located at the coast about 150 km to the west-southwest of SGE (see Fig. 1). A long-term characterization of the regional lower troposphere that is based on these upper-air observations can be found in Muñoz et al. (2011).

c. Down-valley flow indices

The observational characterization presented in section 3 is based upon indices that describe the intensity, directional persistence, jet nose height, and stability of the nocturnal flows observed at the three sites. These indices are defined and justified next.

At the three sites considered, the daytime and nighttime low-level wind regimes are strongly differentiated, as shown by the mean diurnal cycles of 40-m wind speed shown in Fig. 4a. The nighttime phase of the wind regime begins a few hours after sunset, at around 2100 LT, when wind speeds start to intensify; and speeds attain maximum mean values by sunrise, at about 0700 LT. The daytime phase, on the other hand, has maximum

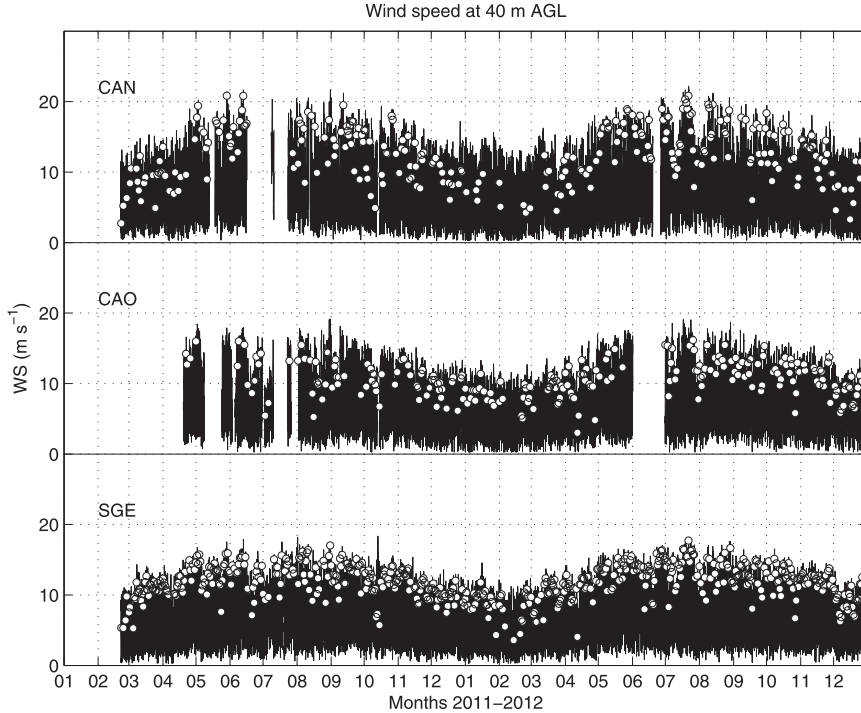


FIG. 3. Continuous lines show the complete time series of hourly averaged wind speed measured at 40 m AGL at stations (top) CAN, (middle) CAO, and (bottom) SGE. White circles correspond to 0200–0600 LT averages for down-valley jet cases (see text). Measurements at all stations started in February 2011, although at CAO wind measurements at 40 m and above were operational only from April 2011 onward.

speeds between 1500 and 1800 LT. Wind directions also show strong contrasts between day and night regimes, as illustrated by the most frequent directions represented with circles in Fig. 4a. At CAN, nighttime (daytime) flow is predominantly from the north-northeast (southwest), while at CAO and SGE the corresponding directions are from the east-northeast (west). On the basis of the well-defined and regular diurnal pattern of near-surface winds, the 0200–0600 LT period is chosen as representative of well-developed nighttime flows.

Figures 4b–d show the joint wind speed–wind direction frequency distribution at 40 m AGL for all observations in the 0200–0600 LT period. The very marked directional preference of the nighttime flow is evident in these figures with 81%, 92%, and 94% of the observations at these hours falling into a 45° sector centered at 10°, 75°, and 80° for stations CAN, CAO, and SGE,

respectively. We shall call these sectors down-valley direction sectors and define, for each night and site, the index FDV40 as the fraction of 40-m wind direction observations in the 0200–0600 LT period that fall into the corresponding down-valley direction sector. Values of FDV40 are generally high, which is indicative of the large topographic control of these nocturnal flows. The wind intensity, however, is more variable, as shown by the wind speed ranges in Figs. 4b–d), with 10-min averages that vary generally between 5 and 20 m s^{-1} . The simple average of 40-m wind speed in the 0200–0600 LT (WS40) period will be used in section 3a as an intensity index for the nocturnal flows at each site (their variability has been shown in Fig. 3). In sections 3b and 3c, on the other hand, the 40-m down-valley projected wind speed (DVWS40) will be used as an index that is better suited for comparing down-valley flow intensities among the different sites.

TABLE 1. Measurement heights and main NRG Systems, Inc., sensors available on 80-m towers.

Variable	Heights (m AGL)	Sensors	Main characteristics
Wind speed	10, 20, 40, 60, and 80	NRG #40C	3-cup anemometer; 0.78 m s^{-1} threshold; 3.0-m distance constant
Wind direction	10, 40, and 80	NRG #200P	Continuous rotation potentiometer; 1.0 m s^{-1} threshold
Temperature	2, 40, and 80	NRG #110S	Integrated circuit temperature sensor; 10-min thermal time constant

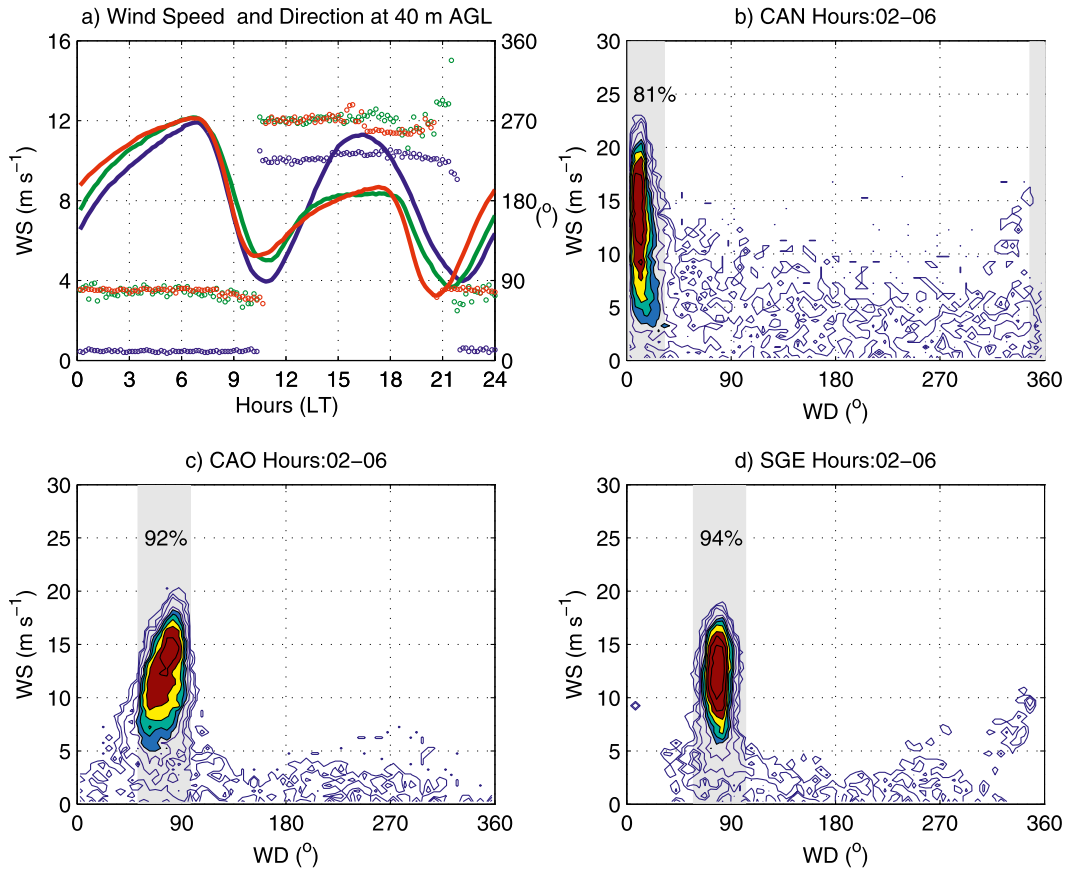


FIG. 4. (a) Diurnal cycles of mean wind speed (solid lines; left scale) and most frequent wind direction (circles; right scale) measured at 40 m AGL for the full period of record at CAN (blue), CAO (green), and SGE (red). Also shown are wind direction–wind speed joint frequency distribution at 40 m AGL for 10-min averages in the 0200–0600 LT period for (b) CAN, (c) CAO, and (d) SGE. Frequency contours are logarithmically spaced to display infrequent occurrences (line contours) and more common occurrences (colored contours). Gray-shaded regions in (b)–(d) mark the down-valley direction sectors as defined for each station. The percentages of 0200–0600 LT wind direction observations falling into this sector are annotated for each site.

The availability of wind speed measurements in the 10–80-m height range has led to the observation that nighttime flows at these sites frequently take the form of a low-level jet, with wind speeds reaching a local maximum at a certain height above the surface. To describe this effect, we define the ZX index as the height of the wind speed maximum for each 10-min observation. Figure 5 shows the frequency distribution of ZX and how it varies in the 1800–0800 LT period. During daytime and at the beginning of the evening transition, ZX corresponds almost always to the highest measurement level, with no indication of a low-level jet; during the night, however, the most common values of ZX are between 20 and 60 m AGL, depending on site and hour. In the early evening the maximum wind speeds are most commonly found in the first measurement level (10 m) at all three stations. As time passes, the nose of the jet profile increases in height, being typically at 20 m at SGE and at

40 m at CAN and CAO, suggesting that the evening wind reversal is a bottom-up process. The nighttime ZX frequency distributions are less variable at SGE, with more variability observed at the other two sites. At CAO, in particular, a secondary maximum is observed after 0200 LT at the 80-m level, indicating that in many cases the nose of the jet is farther aloft or there is no jet structure at all.

The static stability in the tower layer will be described by means of indices computed as 0200–0600 LT averages of the difference of temperatures measured at the upper (DTU = T80 – T40) and lower (DTL = T40 – T02) levels that are equipped with temperature sensors, where T80, T40, and T02 are the temperatures measured at 80, 40, and 2 m AGL. An additional temperature-related index will be the 0200–0600 LT average of the curvature of the temperature vertical profile, estimated as CT = T80 – 2 × T40 + T02.

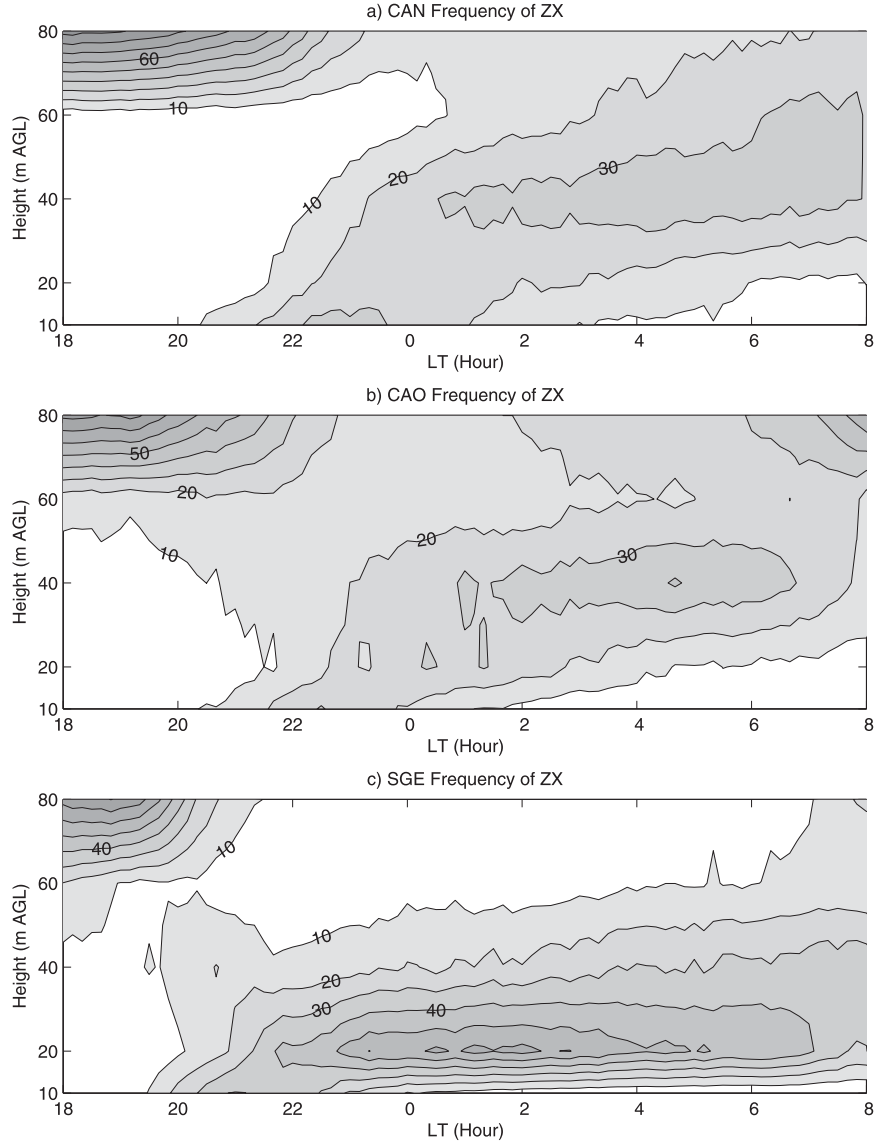


FIG. 5. Time evolution of the frequency distribution of the height of maximum wind speed ZX measured at (a) CAN, (b) CAO, and (c) SGE. Frequency contours are drawn from 10% to 90% at 10% intervals. Only the period from 1800 to 0800 LT is shown with 10-min time resolution. Wind speed data are available only at measuring heights of 10, 20, 40, 60, and 80 m AGL. The full period of record at each station has been considered.

3. Results

a. Characterization of down-valley jets and stability

For each site, we define a down-valley, low-level jet (DVJ) case as a night in which the following conditions are met: 1) FDV40 > 85%, that is, more than 85% of the 0200–0600 LT wind direction observations fall into the down-valley direction sector, and 2) ZX < 80 m in more than 85% of the 0200–0600 LT observations. These conditions are fairly strict in demanding persistent down-valley, nose-shaped wind profiles, but they

still permit the inclusion of a significant number of cases, as illustrated by the time series in Fig. 3 and the occurrence frequency of DVJ cases in Fig. 6a. Site SGE has the maximum percentage of cases along the year (79% annual average) while CAN and CAO have bimonthly frequencies between 20% and 60%. It must be stressed that cases that have been left out may also be low-level jets, but they have a larger directional variability or have maximum speeds at 80 m or above (especially at CAO), rendering them less suited for characterizing wind and temperature profiles below and above the jet nose.

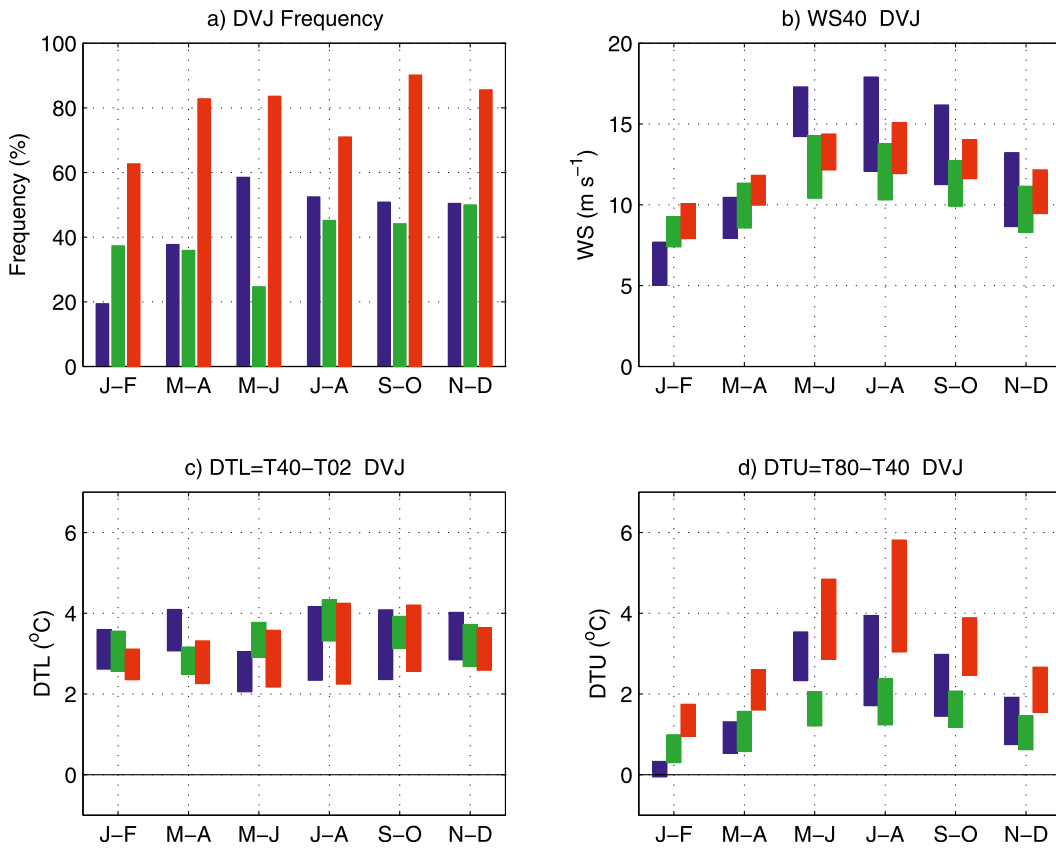


FIG. 6. (a) Bimonthly occurrence frequency of DVJs as defined in the text. Bimonthly variation of interquartile ranges of (b) DVJ intensities at 40 m AGL and temperature difference at (c) 40–2 m and (d) 80–40 m during DVJ events, averaged in the 0200–0600 LT period. In (a)–(d), blue, green, and red colors refer to stations CAN, CAO, and SGE, respectively.

Figure 6b describes the variability of DVJ intensities, as measured by the interquartile ranges of WS40 for each site. Typical magnitudes vary in the 5–18 m s^{-1} range, with an appreciable seasonal modulation that shows larger values between May and October (austral winter and spring). Figures 6c and 6d describe, for DVJ cases, the variability of the stability indices DTL and DTU, respectively. The stability closer to the surface shows little seasonal variation, with temperature differences typically in the 2°–4°C range all year long. The stability in the upper layer, however, has a strong seasonal modulation in phase with the jet intensity (Fig. 6b). This covariability between wind speed and temperature profiles in DVJs is further analyzed next.

To filter out, at least partially, the seasonal covariability of winds and stability, we restrict the subsequent analysis to the months from May to October, which leaves 169, 118, and 300 DVJ cases for CAN, CAO, and SGE, respectively. Figure 7 displays the mean vertical profiles of wind speed and temperature, distinguishing between cases of weak and strong DVJs (using the

median of WS40 as discriminator). A connection between the wind speed and temperature profiles is suggested by Fig. 7, although not as much in terms of the bulk temperature gradient or stability, but rather in terms of the curvature of the temperature profile. Indeed, especially at CAN and SGE, the curvature of the mean temperature profiles changes sign between the weak and strong DVJs. The case-to-case covariability between temperature and wind speed profiles is examined in Fig. 8. At the three sites there is a marked contrast in the relationship between the DVJ intensity and the stability in the lower and the upper layers. Whereas stronger down-valley flows are generally associated with reduced stability in the lower layer, the opposite association exists with the stability in the upper layer. As a result, a positive correlation between the intensity of the flow and the bulk curvature of the temperature profile is observed, as shown in the rightmost scatterplots of Fig. 8. These relationships are clearer at CAN and SGE, in which CT becomes positive in a large number of cases. At CAO, however, only a few cases

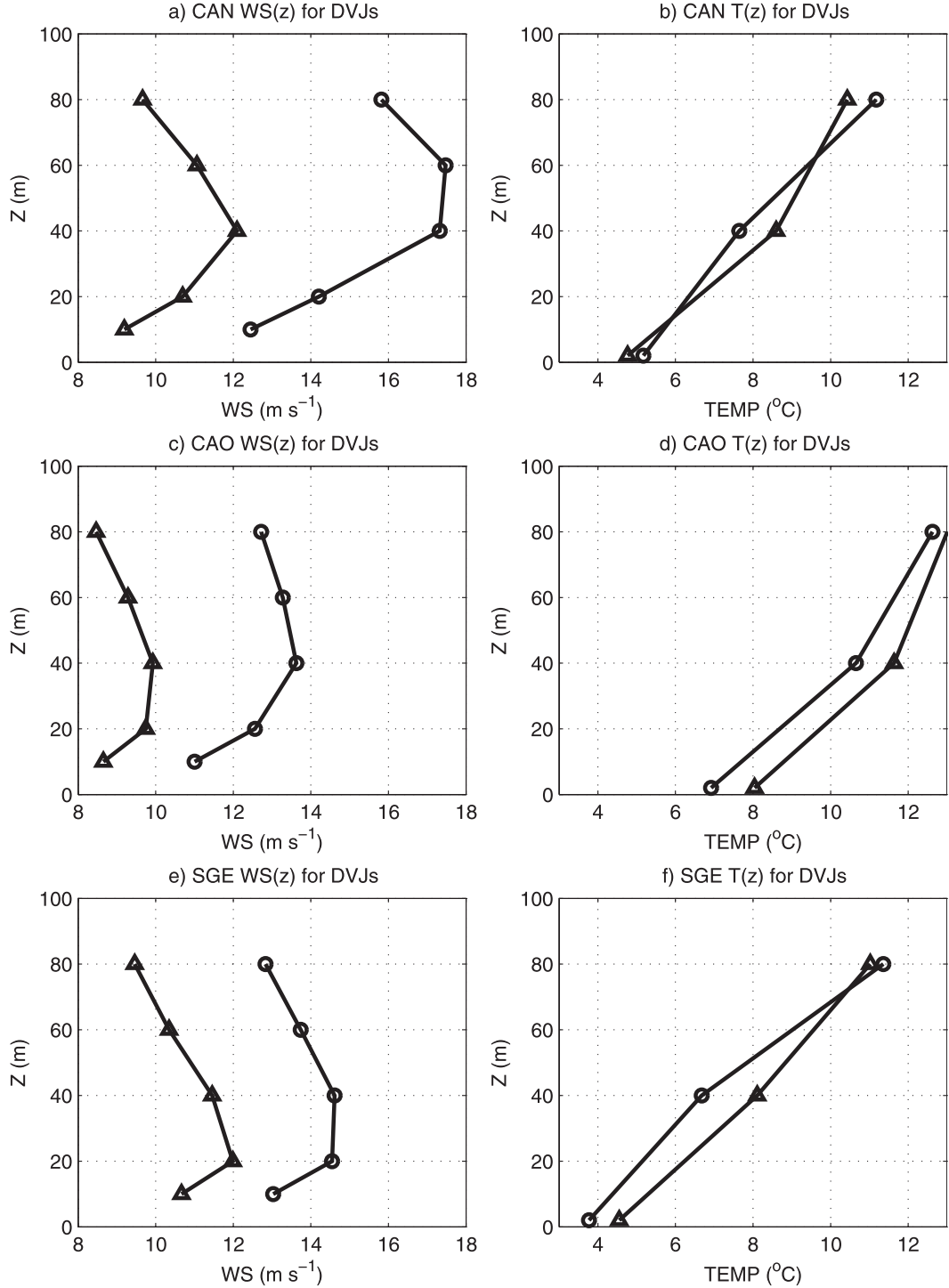


FIG. 7. Vertical profiles, averaged over 0200–0600 LT, of (left) wind speed and (right) temperature averaged over strong (circles) and weak (triangles) DVJs for the months of May–October at stations (a),(b) CAN, (c),(d) CAO, and (e),(f) SGE. The threshold between weak and strong DVJs is based on the median of WS40 at each site (15.4, 11.8, and 13.3 m s^{-1} for CAN, CAO, and SGE, respectively).

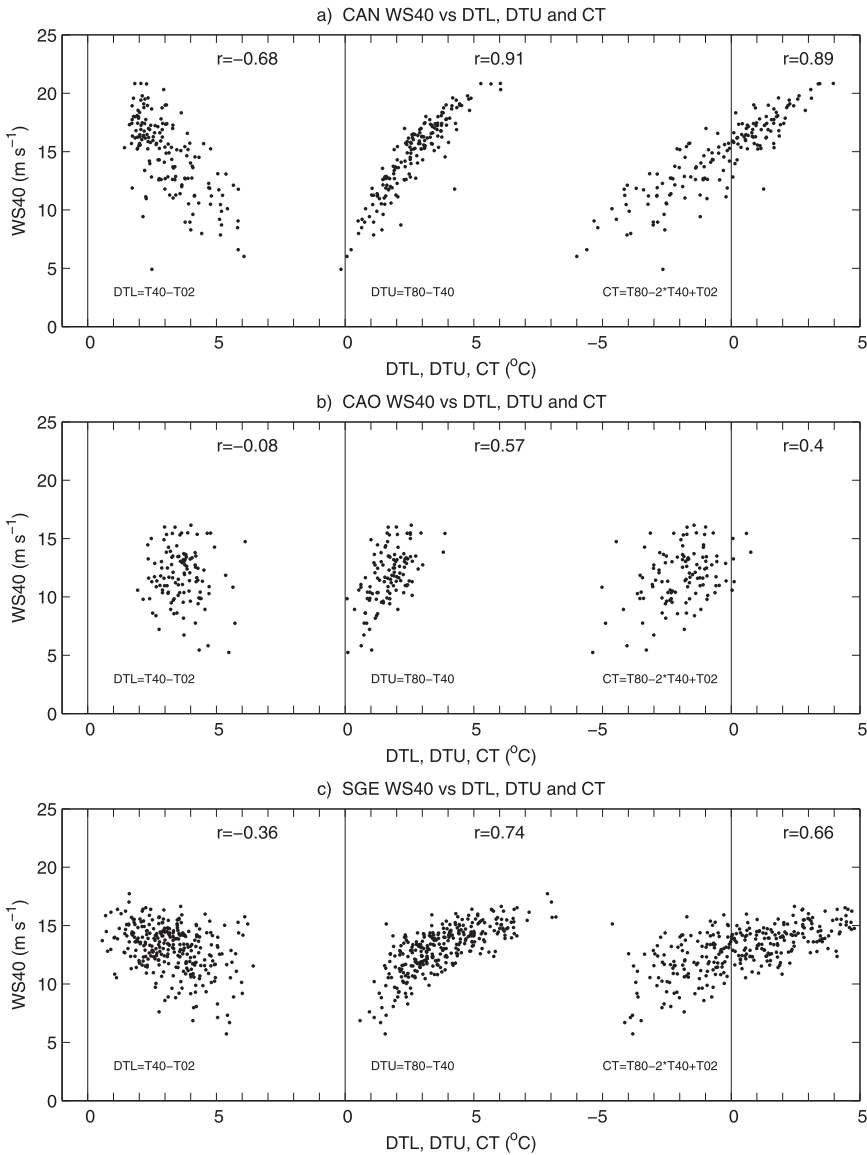


FIG. 8. (a) Dispersion between WS40 and (left) DTL, (center) DTU, and (right) CT for DVJ cases in the months from May to October at the (a), CAN, (b) CAO, and (c) SGE sites. See the text for the definitions of the indices.

reach a positive curvature in the temperature profile. Reasons for the differences among sites have not been elucidated yet, but topographic differences along and across the valleys probably play a role (see Fig. 2).

We interpret the positive correlation between temperature curvature and wind speed as a consequence of the curvature–turbulence relationship proposed by André and Mahrt (1982) (see also Edwards et al. 2006). According to this mechanism, turbulent mixing in the stable boundary layer induces a positive curvature in the temperature profile, opposite to the effect of longwave radiation. Because turbulence may be expected to increase

with stronger low-level winds, this mixing effect might explain the right-hand scatterplots in Fig. 8. Direct measurements of turbulence are unfortunately not available at these towers. As surrogates, we present in Fig. 9 vertical profiles of turbulence-related variables. Figures 9a–c show distributions of gradient Richardson numbers (R_i) that were computed on the basis of the temperature and wind profiles. Three layers can be recognized in these figures. Below the jet nose all three sites show very low R_i values, indicative that in this layer wind shear production can sustain turbulence in the presence of buoyant consumption. The largest values of R_i are found in the

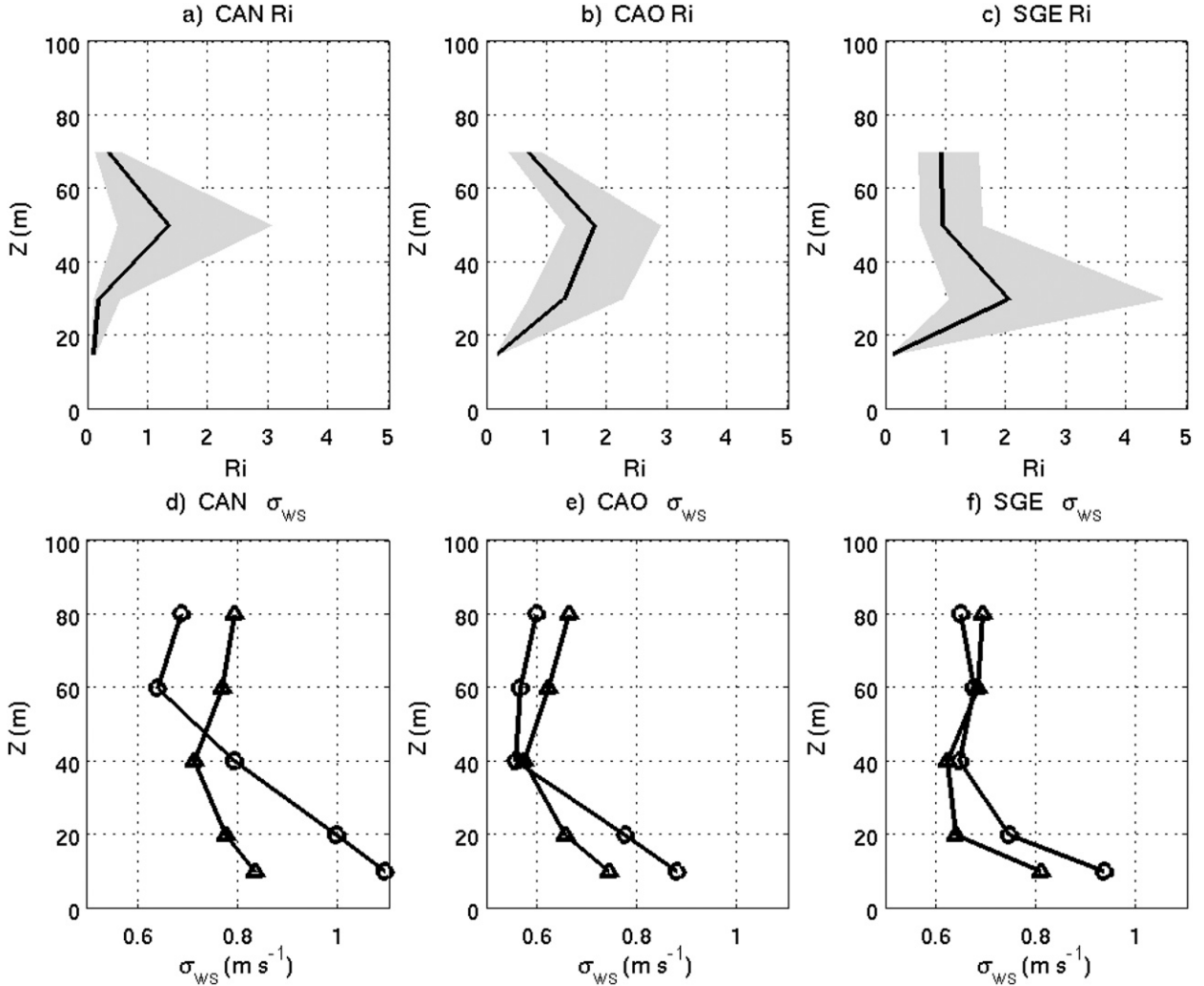


FIG. 9. Vertical profiles of (a)–(c) Richardson numbers during DVJ events (0200–0600 LT averages; shading marks the interquartile range, and the continuous line marks the median values) and (d)–(f) wind speed standard deviation averaged over strong (circles) and weak (triangles) DVJs for stations (left) CAN, (center) CAO, and (right) SGE. The analysis period includes the months from May to October.

region of the jet nose because of the low shear that exists there. Above the jet, where shear is again significant, Ri values are smaller, but not by as much as in the subjet layer (especially at CAO and SGE). Shear production in this layer may not be sufficient to sustain turbulence, although turbulence can still exist if transport from the subjet layer is important. As an approximation to the turbulence intensity in the different layers, Figs. 9d–f show vertical profiles of the standard deviation of wind speed σ_{ws} that is measured by the propeller anemometers, distinguishing again between cases of weak and strong DVJ. Values of σ_{ws} in all levels are comparable, suggesting that turbulence exists throughout the layer sampled by the towers. The largest values of σ_{ws} are found in the lowest measurement levels, consistent with

the smaller Ri values that are found there. The profiles also tend to present a minimum of σ_{ws} at the jet nose level, in accordance again with the small shear production there and the high Ri values. An interesting feature is the change of these mean profiles with DVJ intensity. The stronger down-valley flows are associated with larger values of σ_{ws} in the subjet layer but with smaller values in the layer above the nose. The larger stability existing in this layer associated with the stronger DVJs (see center scatterplots in Fig. 8) may explain this relationship. The overall prevalence of turbulence over the full tower layer and its minimum at the level of the jet that are suggested by these observations are consistent with those reported by Conangla and Cuxart (2006) for a nocturnal jet of $\sim 10 m s^{-1}$ intensity and ~ 65 -m nose height measured

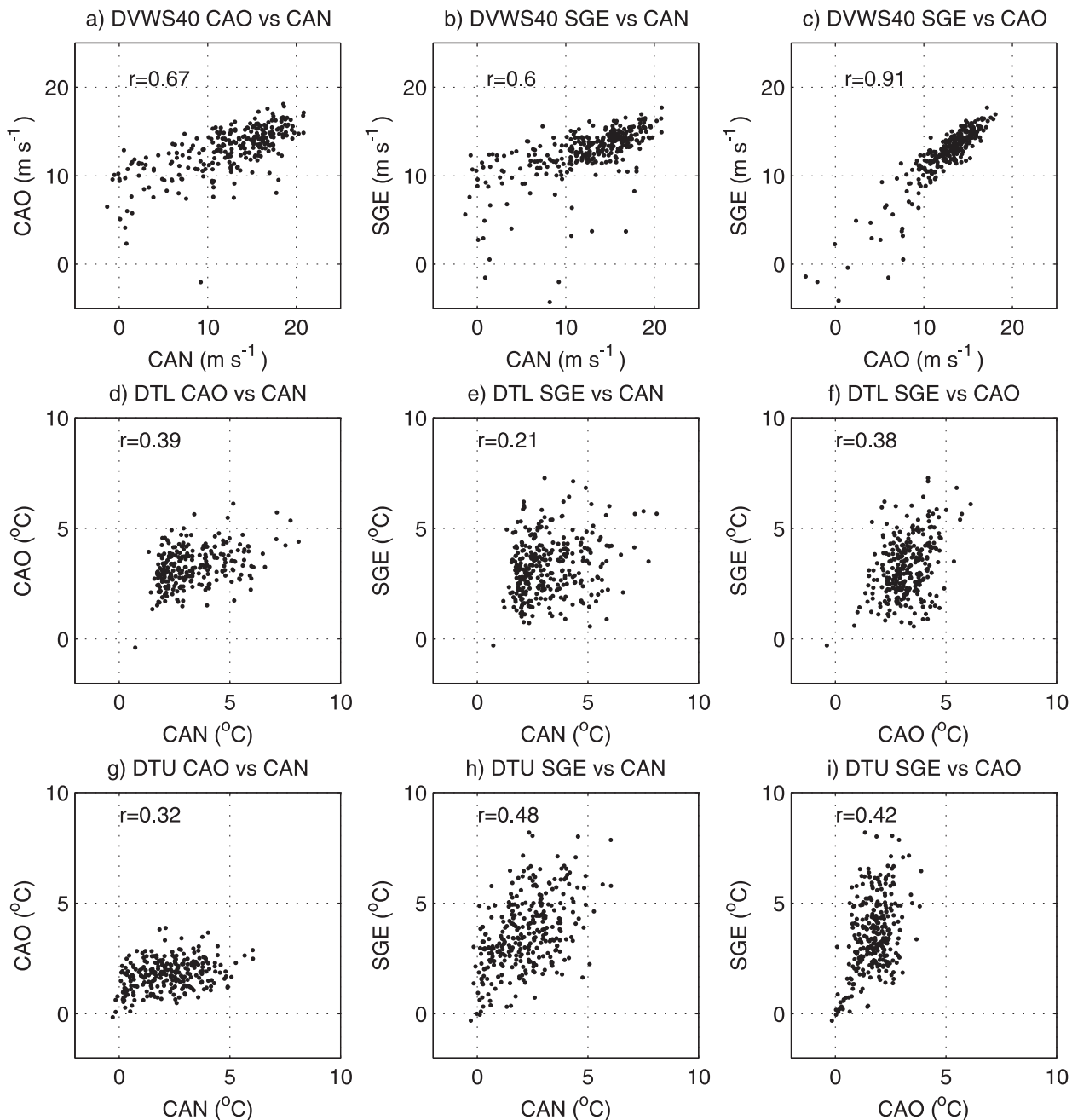


FIG. 10. Covariability of (a)–(c) DVWS40, (d)–(f) DTL, and (g)–(i) DTU among the stations. The analysis period includes the months from May to October.

with a 100-m instrumented tower in the north Castilian Plateau of Spain.

b. Regional control of down-valley flows and temperatures

1) DOWN-VALLEY WINDS

We explore now the covariability of winds among the three sites and with regional forcings. As flow intensity

indices, we consider DVWS40 averaged over 0200–0600 LT for May–October. Figures 10a–c show the scatter diagrams of DVWS40 measured at the three towers. A generally good relationship between the down-valley flow strength at all sites is observed, especially for the high-values range. The best correlation is found between stations CAO and SGE (correlation coefficient r of ~ 0.91), which may be explained by the fact that they are located in contiguous zonally oriented valleys, in contrast to the

TABLE 2. Correlation coefficients between tower measurements and Antofagasta radiosonde data in the 2000–3000 m MSL layer (May–October).

Tower variable	Antofagasta-related variable	CAN	CAO	SGE
DVWS40	ESE-SE wind	0.41	0.53	0.49
DVWS40	TANTO	0.54	0.54	0.62
DVWS40	TANTO-TZNIGHT	0.60	0.71	0.81

meridionally oriented valley of station CAN (see Fig. 2). Therefore, large-scale pressure patterns that modulate down-valley flows in the region may produce a more similar control on CAO and SGE.

The Antofagasta radiosondes provide an opportunity for a first-order evaluation of the large-scale controls on the nocturnal down-valley flows. For this purpose, we computed the correlation coefficients between DVWS40 and three indices derived from the Antofagasta soundings (Table 2). In all cases, the largest correlations are found for Antofagasta variables in the 2000–3000 m MSL range, coincident with the altitudinal range of the 80-m towers. The first row in Table 2 shows the correlation between the down-valley flows at the three sites and the winds measured by the 1200 UTC soundings. To be more specific, the correlation is with the component of the upper-air winds coming from the east-southeast-southeast (ESE-SE) sector, for which the correlation was highest for the three sites. A modest zero-lag correlation of $r \sim 0.5$ is found, with no marked differences among sites.

The second and third rows in Table 2 quantify the relationship between the intensity of the down-valley winds and the free-troposphere temperature structure. The down-valley wind mechanism suggests that the relative cooling of the valley air mass relative to the free troposphere at the same altitude should enhance the drainage winds. Indeed, for the three sites the largest correlations found are those between DVWS40 and the difference between the Antofagasta temperature averaged in the 2000–3000 m MSL layer (TANTO) and the tower temperatures averaged over the three data levels (TZNIGHT). This result suggests that the down-valley wind mechanism may be at work in these flows, especially considering that correlations with the temperature difference generally increase as compared with those calculated using the radiosonde temperature alone (comparing values from the second and third rows in Table 2). Nonetheless, all of these correlations are relatively modest, and the scatterplots associated with them display a large dispersion (not shown), which may be partially explained by the ~200-km distance between Antofagasta and the tower sites.

2) TEMPERATURE PATTERNS

Figures 10d–f and 10g–i respectively show the scatter diagrams between DTL and DTU values among the three sites. The correlations in these cases are smaller than in the case of the flow strengths, suggesting that the adjustment of the temperature profile to the down-valley flow is influenced by local factors. In this regard, the small range of stabilities measured at CAO in comparison with CAN and SGE could be related to the presence of the city of Calama upwind of CAO. The large roughness associated with the urban land use may preclude the development of intense inversions near the surface.

In terms of the temperature comparison among the different sites, a noticeable feature apparent in Fig. 7 is the higher temperatures in CAO as compared with its up-valley counterpart CAN. While the down-valley mechanism requires colder temperatures upwind at the same altitude, near the surface the temperature usually drops in the down-valley direction, especially if the topography forces the drainage flow to accumulate and form cold pools. In our case, Figs. 7b–f show that the down-valley site CAO has a near-surface temperature that is approximately 2.5°C higher than that measured at CAN. To understand better this regional temperature pattern, Fig. 11 shows the average nighttime temperatures measured at the three 80-m towers as a function of altitude. We have also included in the figure the corresponding 5-m-averaged temperatures at four additional 20-m towers that exist in the same valleys (locations are shown in Fig. 2). The general trend of warmer temperatures at lower sites is confirmed by all stations, provided that the different heights above the ground of the measurements and the different valleys of each station are taken into account. The continuous vertical profile in Fig. 11 shows the corresponding temperature average of the 1200 UTC (0800 LT) operational radiosonde measurements that are available at the coast in Antofagasta (see Fig. 1). The well-defined subsidence inversion very frequently observed at this location leaves a clear hallmark in the mean temperature profile, characterized by a conspicuous inversion in the 800–1500-m layer (Muñoz et al. 2011). The subsidence inversion, however, rarely exceeds 2000 m MSL, leaving the altitude range occupied by the analyzed stations under the influence of the free troposphere above the inversion. Indeed, the mean lapse rate of the radiosonde profile is very close to that of the surface stations. Moreover, while the nighttime near-surface measurements are considerably colder than the radiosonde profile at the same altitude, the 80-m measurements are much closer, suggesting that the surface inversions in these valleys tend to match the

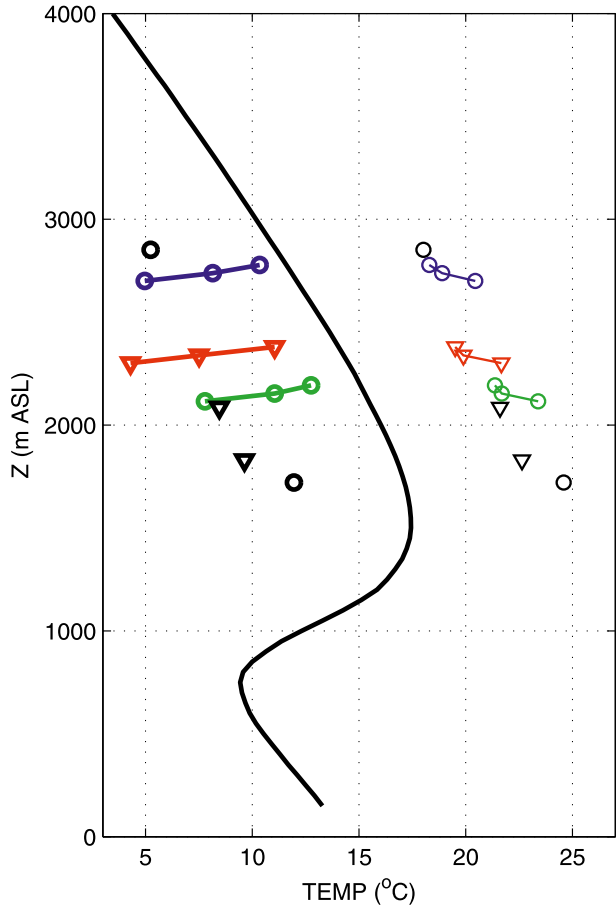


FIG. 11. Temperatures averaged over the months from May to October plotted against the altitude above sea level of the sensor. The black solid line shows 1200 UTC (0800 LT) Antofagasta radiosonde data. Colored profiles are for 0200–0600 LT (thick lines and symbols) and 1400–1800 LT (thin lines and symbols) averages at CAN (blue), CAO (green), and SGE (red). The black symbols indicate 0200–0600 LT (thick) and 1400–1800 LT (thin) averages of 5-m temperatures measured at 20-m meteorological masts (at locations shown in Fig. 2). Triangles and circles indicate stations located along Arriero Creek and Loa River valleys, respectively.

free-tropospheric temperature (if one keeps in mind the differences in the times of the station temperatures and the upper-air temperatures in Fig. 11). These observations suggest that the turbulent mixing associated with the strong down-valley flows is capable of keeping the near-surface temperatures in the valleys coupled to the free-tropospheric thermal profile.

c. Slope-cooling forcing of down-valley flows

In the previous section, we assessed the down-valley wind mechanism as a factor of the observed nocturnal flows by relating them to the regional wind and thermal structure. While some support for the down-valley mechanism was found, this observational work would

not be complete without an estimate of the slope-wind mechanism as well. As pointed out in section 1, real complex-terrain winds are prone to be affected by various factors in different degrees, and, given the significant slope of these valley axes ($\sim 1.5\%$; see section 2), the cooling of the sloping surface air might play a role as well.

Figures 12a and 12b show the mean evolution of the down-valley component of the wind and the near-surface stability at the three sites. The existence of two distinct phases during nighttime is suggested by these plots. A transition phase occurs between 1800 and 0200 LT in which the down-valley flow intensity increases steadily (Fig. 12a). Afterward, between 0200 and 0700 LT, a quasi-stationary regime of flow and stability is observed. The evolution of the stability at 40 – 2 m during the transition phase shows an interesting behavior (Fig. 12b). It changes sign at sunset (1800 LT), just before the time at which the down-valley flows begin to increase, and then it reaches a maximum in the middle of the transition; it finally adjusts to a lower value in the quasi-stationary phase. Although the details of the transitions are different at each station, the initial and final states and the shape of the transition are similar for the three of them. The joint evolution of down-valley flow and stability during the transition suggests a mutual adjustment. Development of the surface inversion appears to accelerate the flow in the down-valley direction, with the flow at some time becoming so intense that its accompanying turbulent mixing reduces the near-surface stability, and a kind of equilibrium between stability and flow strength is finally established.

Some quantification of the slope mechanism is possible from the available observations. To do so, we compute the down-valley pressure gradient driven by a surface temperature inversion over a sloped surface. Let us model the temperature inversion as

$$T(z) = T_{\infty} - \Delta_o \exp(-z/H), \quad (1)$$

where T_{∞} is the upper-air temperature, Δ_o represents the intensity of the surface cooling, H is the height scale of the inversion, and z is the local vertical coordinate. The hydrostatic equation applied to this temperature structure results in

$$\frac{dp}{dz} = -\frac{gp}{RT_{\infty}} \left[1 - \frac{\Delta_o}{T_{\infty}} \exp(-z/H) \right]^{-1}, \quad (2)$$

where g is the acceleration of gravity and R is the ideal gas constant for air. The three parameters T_{∞} , Δ_o , and H are assumed to be uniform in space so that horizontal pressure gradients arise solely as a result of the along-slope

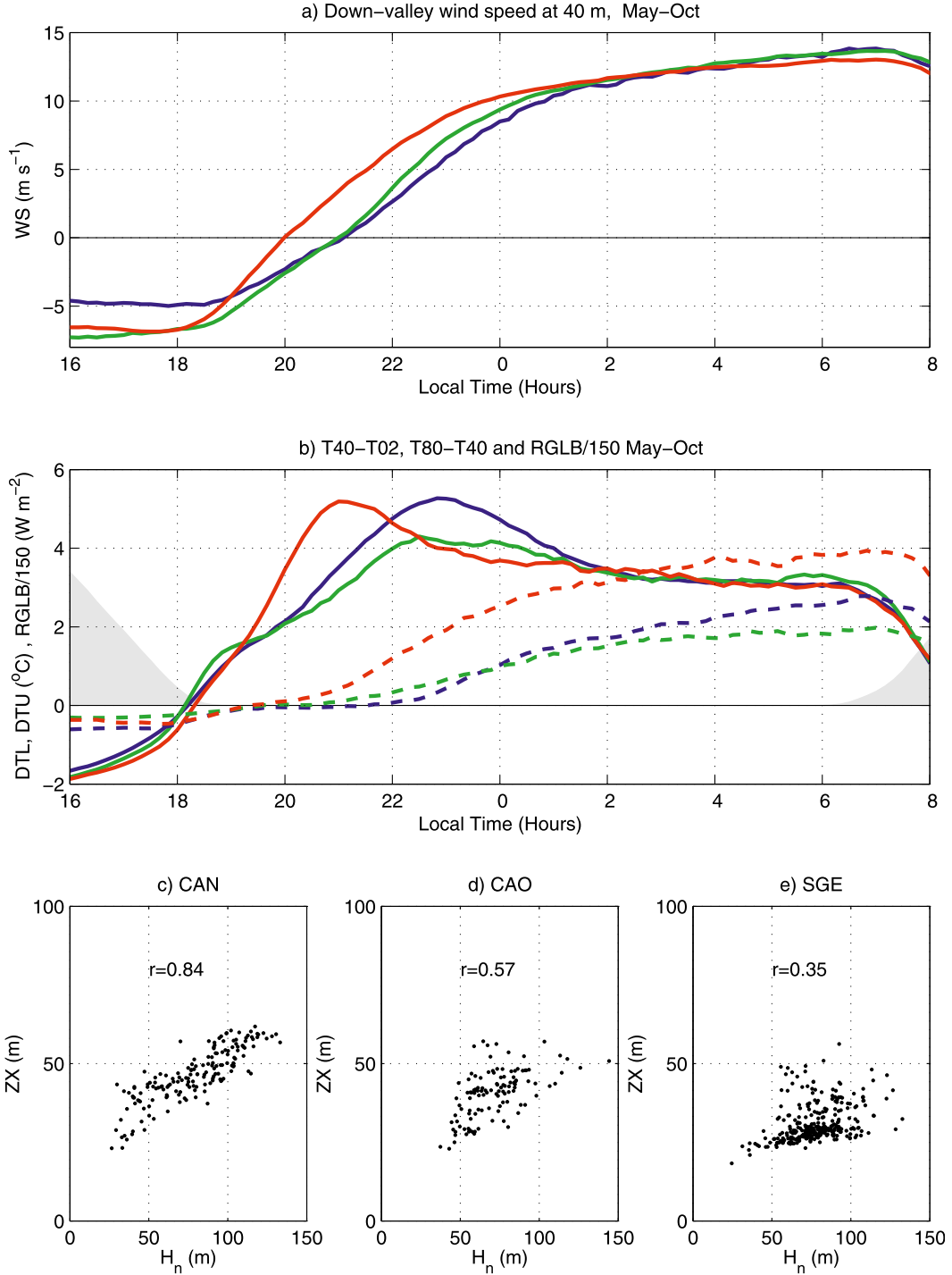


FIG. 12. (a) May–October average of down-valley projected wind speed at 40 m AGL for stations CAN (blue line), CAO (green line), and SGE (red line) for the period between 1600 and 0800 LT. (b) As in (a), but for temperature difference at 40 – 2 m (solid lines), temperature difference at 80 – 40 m (dashed lines), and mean surface solar radiation scaled by 150 (shaded areas). Also shown are scatterplots between observed jet nose heights ZX and estimates that are based on Eq. (6) for stations (c) CAN, (d) CAO, and (e) SGE. To have a continuous estimate of ZX , a second-order polynomial was fitted to the three data levels around the observed wind speed maximum.

change of altitude Z for a constant value of z , as given by $Z = Z_T(x) + z$, where Z_T is the surface altitude and x is the distance coordinate in the up-valley direction. If one assumes a small slope $s = dZ_T/dx$ and small perturbations with respect to density ρ_o and temperature T_o , the horizontal pressure gradient at the surface in the up-valley direction is approximately

$$\frac{1}{\rho_o} \frac{\partial p}{\partial x} \sim sg \frac{\Delta_o}{T_o}. \quad (3)$$

If we estimate Δ_o from the T40 – T02 difference shown in Fig. 12b, then its linear time increase during the transition can be approximated by $\Delta_o \sim [5^\circ\text{C} (4\text{ h})^{-1}]t$, where t is time after sunset. Replacing this expression in Eq. (3) and integrating in time for a 4-h transition, we obtain that the pressure gradient can support an increase of 18 m s^{-1} in the downslope flow in the 4 h (we have used $s \sim 0.015$ and $T_o \sim 300 \text{ K}$). This value is large but is of the same order as the $\sim 12 \text{ m s}^{-1}$ observed increase in downslope flow during the transition (Fig. 12a), the overestimation suggesting that turbulent friction plays a role as well. Indeed, the role of turbulence is presumably important after the stability and flow have mutually adjusted. If we assume that in the quasi-stationary regime a balance exists between the turbulence and pressure gradient forces, then

$$\frac{\partial \overline{u'w'}}{\partial z} \sim -sg \frac{\Delta_o}{T_o}, \quad (4)$$

where $\overline{u'w'}$ is the turbulent momentum flux. The left-hand side of Eq. (4) can be estimated as

$$\frac{\partial \overline{u'w'}}{\partial z} \sim -\frac{u_*^2}{H_n}, \quad (5)$$

where u_* is the surface friction velocity and H_n is a height scale at which $\overline{u'w'} \sim 0$. By combining Eqs. (4) and (5), an estimate for H_n is obtained:

$$H_n \sim u_*^2 \left(sg \frac{\Delta_o}{T_o} \right)^{-1}. \quad (6)$$

The friction velocity can in principle be related to the wind speed at 10 m AGL using atmospheric surface layer relationships. During the quasi-stationary regime, wind speed at 10 m AGL is $\sim 10 \text{ m s}^{-1}$ (Fig. 7), and, if one assumes near-neutral conditions in the surface layer, we can estimate u_* by using a logarithmic wind profile and a surface roughness appropriate for a desert ($z_o \sim 10^{-3} \text{ m}$), obtaining $u_* \sim 0.4 \text{ m s}^{-1}$. Figure 12b shows that

in the equilibrium $\Delta_o \sim 5^\circ\text{C}$ (we include also the temperature difference between 80 and 40 m, which in the equilibrium regime is significant), so that the scale height $H_n \sim 65 \text{ m}$. This scale is higher but is of the same order as the observed height of the jet nose (between 20 and 60 m AGL according to Fig. 5) at which, by symmetry arguments, $\overline{u'w'}$ can indeed be argued to be close to zero, consistent also with the turbulence modeling of nocturnal jets by Conangla and Cuxart (2006) and Cuxart and Jiménez (2007). Two reasons can be thought of to explain the overestimation of H_n with respect to the observed nose jet heights: 1) the neutral assumption in the estimation of u_* probably produces an overestimation of u_* , given that near-surface conditions are more stable than neutral; 2) if the actual H_n is in the 20–40 m AGL range, then wind speed measurements at 10 m AGL probably fall outside the atmospheric surface layer (conventionally defined as the layer in which turbulent fluxes change by less than 10% from their surface values) so that the u_* estimate that is based on the 10-m wind speed is again questionable. Neither of these two considerations, however, invalidates the interpretation of Eq. (6) as an estimate for the nose height scale of an equilibrium turbulent down-slope jet. Application of Eq. (6) to explain the observed case-to-case variability of ZX produces the scatterplots in Figs. 12c–e. While the overestimation of nose height values persists, a positive correlation between H_n and ZX is found at the three sites, being largest at CAN, where about 70% of the observed ZX variance is explained by Eq. (6).

To summarize this section, we conclude that, during the transient phase and during the quasi-equilibrium regime of these down-valley flows, the joint evolution of the stability and the flow intensity suggests that the down-slope pressure gradient due to the surface cooling and the turbulent wind stress are both important terms in their momentum budgets.

4. Summary and conclusions

To the authors' knowledge, this communication provides the first extended ($\sim 2 \text{ yr}$, 0–80 m AGL, and three sites) documentation of the surface wind flow over the Atacama Desert region of northern Chile. The most conspicuous feature of the observed wind regime is the existence of a strong nocturnal drainage flow with hourly averaged down-valley speeds reaching up to about 20 m s^{-1} during the cold season. The multilevel measurements reveal nose-shaped wind profiles with maximum values occurring at about 20–60 m AGL. The frequency of occurrence of persistent down-valley nocturnal jets with a well-defined nose-shape profile in the 0–80-m layer shows little seasonal preference. Their

intensity, however, shows a marked seasonality, with stronger flows occurring between May and October. Stronger down-valley jets are associated with a more positive curvature of the temperature profile, probably because of the effect of turbulent mixing. Standard deviation of wind speed suggests that strong turbulence prevails in the full tower layer, despite gradient Richardson numbers being large at the jet nose and above it.

Turbulent mixing also appears to be responsible for the warmer temperatures observed at the lower-altitude sites down the valleys. In fact, the mean altitudinal lapse rate of near-surface temperature matches closely the free-tropospheric lapse rate measured at an aerological station located at the coast. Regressions between these upper-air measurements and the tower observations show that there exists a moderate control of valley nocturnal flows by large-scale factors. The highest correlations found are those between the down-valley flow intensity and the temperature difference between the free troposphere and the valley, providing some support for the down-valley wind mechanism. Nevertheless, estimates of terms in the momentum budget for the development and quasi-stationary phases of the down-valley flows suggest that the pressure gradient force due to the near-surface cooling along the sloping valley axes also plays an important role in these drainage flows. A scale for the height of the wind speed maximum in equilibrium turbulent down-slope jets is proposed on the basis of the surface friction velocity and the surface inversion intensity. At site CAN, this scale explains about 70% of the case-to-case variance of the observed jet nose height, although a significant overestimation is found, probably as a result of an overestimation of the friction velocity.

The flow system reported here has immediate importance in the characterization of the wind-energy potential of the Atacama Desert. As mentioned in section 1, these measurements were undertaken by the Chilean government to explore the possibility of wind-farm development in the Atacama region, where the current demand for energy is particularly high. Our results show that, while there is possibly a good wind resource at all measurement sites, the shape and the relationship with stability of the vertical profiles of wind speed sustained by these flows can be very different from what is commonly found in wind-farm sites over flat terrain (e.g., van den Berg 2008)—a fact that must be properly taken into account in the evaluation and design of future wind-energy projects in this area. Beyond this applied aspect, further studies should better define the spatial structure and organization of the nocturnal circulation to assess how representative these measurements are of the general low-level wind regime of the Atacama Desert. Additional investigations should better characterize the

evening and morning transitions of these winds and their turbulent structure as well as elucidate their possible interaction with the coastal boundary layer and subsidence inversion existing to the west and quantify their potential role in the zonal transport of natural and anthropogenic aerosols from the continent to the SEP stratocumulus layer existing offshore. Studies on the numerical modeling and the synoptic forcing of these flows are currently under way to address some of these issues.

Acknowledgments. This research was funded by a co-operation agreement between the University of Chile and the Chilean Ministry of Energy under Exempt Decree 249 of 2013. The measurement campaign in northern Chile was carried out by programs of the Chilean Ministry of Energy, with partial support from the German GIZ Agency (Deutsche Gesellschaft für Internationale Zusammenarbeit GmbH). Special thanks are given to Mr. Christian Santana, then at the Ministry of Energy, for the energy he put into initiating these measurement programs. The authors thank four anonymous reviewers for suggestions that improved the paper.

REFERENCES

- André, J. C., and L. Mahrt, 1982: The nocturnal surface inversion and influence of clear-air radiative cooling. *J. Atmos. Sci.*, **39**, 864–878.
- Bromwich, D. H., 1989: An extraordinary katabatic wind regime at Terra Nova Bay, Antarctica. *Mon. Wea. Rev.*, **117**, 688–695.
- Chand, D., D. A. Hegg, R. Wood, G. Shaw, D. Wallace, and D. Covert, 2010: Source attribution of climatically important aerosol properties measured at Paposo (Chile) during VOCALS. *Atmos. Chem. Phys.*, **10**, 10 789–10 802.
- Conangla, L., and J. Cuxart, 2006: On the turbulence in the upper part of the low-level jet: An experimental and numerical study. *Bound.-Layer Meteor.*, **118**, 379–400.
- Cuxart, J., and M. A. Jiménez, 2007: Mixing processes in a nocturnal low-level jet: An LES study. *J. Atmos. Sci.*, **64**, 1666–1679.
- Edwards, J. M., R. J. Beare, and A. J. Lapworth, 2006: Simulation of the observed evening transition and nocturnal boundary layers: Single-column modelling. *Quart. J. Roy. Meteor. Soc.*, **132**, 61–80.
- Garreaud, R., 2010: The Andes climate and weather. *Adv. Geosci.*, **7**, 1–9.
- , and P. Aceituno, 2007: Atmospheric circulation and climatic variability. *The Physical Geography of South America*, A. Orme, T. T. Veblen, and K. Young, Eds., Oxford University Press, 45–59.
- , A. Molina, and M. Farías, 2010: Andean uplift, ocean cooling and Atacama hyperaridity: A climate modeling perspective. *Earth Planet. Sci. Lett.*, **292**, 39–50.
- Mahrt, L., 1982: Momentum balance of gravity flows. *J. Atmos. Sci.*, **39**, 2701–2711.
- Muñoz, R., R. A. Zamora, and J. A. Rutllant, 2011: The coastal boundary layer at the eastern margin of the southeast Pacific (23.4°S, 70.4°W): Cloudiness-conditioned climatology. *J. Climate*, **24**, 1013–1033.

- Parish, T., 1982: Surface airflow over East Antarctica. *Mon. Wea. Rev.*, **110**, 84–90.
- , and D. Bromwich, 1987: The surface windfield over the Antarctic ice sheets. *Nature*, **328**, 51–54.
- Rutllant, J., and P. Ulriksen, 1979: Boundary-layer dynamics of the extremely arid northern part of Chile. *Bound.-Layer Meteor.*, **17**, 41–55.
- , H. Fuenzalida, and P. Aceituno, 2003: Climate dynamics along the arid northern coast of Chile: The 1997–1998 Dinamica del Clima de la Región de Antofagasta (DICLIMA) experiment. *J. Geophys. Res.*, **108**, 4538, doi:10.1029/2002JD003357.
- Savage, L. C., III, S. Zhong, W. Yao, W. J. O. Brown, T. W. Horst, and C. D. Whiteman, 2008: An observational and numerical study of a regional-scale downslope flow in northern Arizona. *J. Geophys. Res.*, **113**, D14114, doi:10.1029/2007JD009623.
- Schmidli, J., and Coauthors, 2011: Intercomparison of mesoscale model simulations of the daytime valley wind system. *Mon. Wea. Rev.*, **139**, 1389–1409.
- Schmidt, D., 1999: *Das Extremklima der nordchilenischen Hochatacama unter besonderer Berücksichtigung der Höhengradienten (The Extreme Climate of the Northern Chilean High Atacama with Special Reference to the Altitudinal Gradient)*. Dresdener Geographische Beiträge, Vol. 4. Technische Universität Dresden, 122 pp.
- van den Berg, G. P., 2008: Wind turbine power and sound in relation to atmospheric stability. *Wind Energy*, **11**, 151–169.
- Wendler, G., C. Stearns, G. Weidner, G. Dargaud, and T. Parish, 1997: On the extraordinary katabatic winds of Adelie Land. *J. Geophys. Res.*, **102**, 4463–4474.
- Whiteman, C. D., 1990: Observations of thermally developed wind systems in mountainous terrain. *Atmospheric Processes over Complex Terrain, Meteor. Monogr.*, No. 45, Amer. Meteor. Soc., 5–42.
- , 2000: *Mountain Meteorology: Fundamentals and Applications*. 1st ed. Oxford University Press, 355 pp.
- , and J. C. Doran, 1993: The relationship between overlying synoptic-scale flows and winds within a valley. *J. Appl. Meteor.*, **32**, 1669–1682.
- , and S. Zhong, 2008: Downslope flows on a low-angle slope and their interactions with valley inversions. Part I: Observations. *J. Appl. Meteor. Climatol.*, **47**, 2023–2038.
- Wolter, K., and M. S. Timlin, 2011: El Niño/Southern Oscillation behaviour since 1871 as diagnosed in an extended multivariate ENSO index (MEI.ext). *Int. J. Climatol.*, **31**, 1074–1087.